Available online at www.sciencedirect.com
ScienceDirect
Trans. Nonferrous Met. Soc. China 35(2025) 701−714
Transactions of Nonferrous Metals Society of China
www.tnmsc.cn

Wire arc additive manufacturing of Al−Si−Mg aluminum alloy through wire−powder synchronous deposition

Yun-fei MENG[1,2], Qian-xi YU[1,2], Xu WU[1,2], Ming GAO[3], Hui CHEN[1,2]

1. School of Materials Science and Engineering, Southwest Jiaotong University, Chengdu 610031, China;
2. Key Laboratory of Advanced Technologies of Materials, Ministry of Education, Southwest Jiaotong University, Chengdu 610031, China;
3. Wuhan National Laboratory for Optoelectronics, Huazhong University of Science and Technology, Wuhan 430074, China

Received 2 August 2023; accepted 3 January 2024

Abstract: Owing to the lack of matching commercial welding wires, the development of wire arc additive manufacturing (WAAM) for most aluminum alloys is hindered. A wire−powder synchronous arc additive manufacturing (WPAAM) was proposed to prepare the target Al−Si−Mg aluminum alloy. Based on the synchronous deposition of $AlSi_{12}$ wire and pure Mg powder, the deposition width of the WPAAMed thin-wall was increased by 61% compared with that of WAAMed thin-wall using $AlSi_{12}$ wire, and the machining allowance was reduced by 81%. The added Mg powder benefited to form refined equiaxed grains, and reduced the average grain size of the WPAAMed thin-wall to 47.1 μm, showing a decrease of 23.8% relatively to that of the WAAMed thin-wall. Besides, Mg reacted with Si to form Mg_2Si strengthening phases. The mechanical properties tests showed that the ultimate tensile strength and elongation of the WPAAMed thin-wall increased up to 174.5 MPa and 4.1%, reaching 92% and 60% those of the WAAMed thin-wall, respectively.

Key words: wire arc additive manufacturing; wire-powder synchronous deposition; Al−Si−Mg aluminum alloy; forming accuracy; mechanical properties

1 Introduction

Al−Si aluminum alloys account for more than 80% of the total amount of cast aluminum alloys due to their good fluidity, small hot tearing tendency, and high air tightness. The added eutectic Si helps to improve the fluidity of aluminum alloy [1−3]. However, too high Si content also forms laminar or even block eutectic Si, which seriously splits the Al matrix and decreases its strength and toughness. Therefore, Mg, Mn, Cu and other elements are usually introduced into the Al−Si aluminum alloy. For example, by adding Mg element, a new phase of Mg_2Si can be formed while maintaining the advantages of Al−Si alloys, and the solid solution−precipitation strengthening effect could be obtained [4−6]. The Al−Si−Mg aluminum alloys are widely used in many medium-load parts, such as the heat exchanger, gearbox shell, and engine cylinder.

Al−Si−Mg aluminum alloy parts are usually manufactured in batches by the casting or forging, while some complex structures require the machining and welding cooperation. However, with the rapid development of lightweight structure and functional integration in the aerospace, rail transit and new energy vehicles, these traditional methods

Corresponding author: Yun-fei MENG, Tel: +86-28-87600267, E-mail: yfmeng@hotmail.com;
Ming GAO, Tel: +86-27-87793402, E-mail: mgao@hust.edu.cn
DOI: https://doi.org/10.1016/S1003-6326(24)66709-9

could not meet the design requirements for the small- and medium-sized complex components. There are some problems such as the slow response, long cycle, large material waste, and high cost. Additive manufacturing (AM) is based on the principle of discrete-stacking, and benefits to realize the direct processing and rapid manufacturing from three-dimensional models to solid parts [7−9]. The AM has the advantages of high efficiency and flexibility, and can fully meet the new needs and developments of metal parts manufacturing [10−13].

With the increase of Si content, the sharp-angled flake or even coarse blocky eutectic Si easily forms in the Al−Si−Mg aluminum alloys, which seriously splits the Al matrix. During the wire drawing, the formed block eutectic Si results in the wire fracture owing to induced stress concentration. As a result, the wire fabrication for Al−Si−Mg aluminum alloy is hindered. The existing AM for Al−Si−Mg aluminum alloy is mainly carried out by the powder-based selective laser melting or direct energy deposition [14−16]. However, there are still some problems existing in the laser additive manufacturing, such as the low laser absorption rate, poor powder fluidity, serious oxidation, and excessive temperature gradient. Especially when forming the large-sized batch components, the laser additive manufacturing faces the low powder utilization rate, long manufacturing cycle, and high production cost [17−19].

Wire arc additive manufacturing (WAAM) originates from arc welding with high deposition efficiency and low manufacturing cost [20−23]. The WAAM uses arc as the heat source and is based on wire forming, which avoids the problems of easy oxidation, high cost, and low efficiency based on powder forming [24,25]. Previous studies [26−29] have proved that, the forming size of WAAM could reach 3000 mm × 3000 mm × 2000 mm, and the material utilization rate is larger than 90%. In addition, the post-processing could be adopted to obtain functional surfaces when fabricating the parts with complex structures. However, the WAAM researches for most aluminum alloys are hindered by the lack of matching welding wires. Some researchers tried to use a multi-wire combination WAAM to solve the above problems [30,31]. However, due to the limitation of both the commercial wire types and the wire feeding rate, the adjustable range of target alloy composition is limited. For example, QI et al [30] obtained only Al−3.1Mg−2.0Si alloy through the WAAM by simultaneously filling $AlMg_5$ and $AlSi_5$ welding wires.

Therefore, how to solve the problem of alloy composition matching is the key problem faced by the WAAM for most aluminum alloys. To this end, the current study uses a synchronous wire−powder arc additive manufacturing (WPAAM) by optimizing the composition ratio and feeding rate of powder. Based on the synchronous deposition of wire and powder, the high-efficiency and high-performance fabrication of the target Al−Si−Mg aluminum alloys could be realized. In addition, because the arc has the characteristics of low heat flux density and large heating radius, the arc combustion and droplet transfer are easily affected by environmental factors during the WAAM [32−34]. Therefore, another purpose of this study is to explore whether the appropriate powder addition changes the combustion characteristics of arc, improves its energy concentration, and then increases the forming accuracy of WAAM. The related results are expected to enrich the basic theory of WAAMed aluminum alloy, and provide a technical approach for the high-efficiency fabrication of large-sized metal components.

2 Experimental

The ER4047 aluminum alloy with a diameter of 1.2 mm was used as the filling wire during the WPAAM, and the pure Mg and pure Ti with the particle sizes between 150 and 50 μm were adopted as the feeding powders. The substrate used in the deposition was the 6061 aluminum alloy with dimensions of 150 mm × 50 mm × 15 mm. The chemical compositions of the substrate and filler wire are presented in Table 1 [35,36]. The surface of the substrate was firstly ground and cleaned to remove both the oxide films and impurities, and then cleaned with alcohol before the deposition. The substrate, wire, and powders were baked prior to the deposition to remove the potential moisture contamination and hence minimize the porosity near the deposited metal. The argon with high purity was used both for the shielding gas during the arc burning and the carrier gas for the powder feeding.

Table 1 Chemical compositions of substrate and filler wire [35,36]

Material	Content/wt.%								
	Mg	Zn	Mn	Si	Fe	Cu	Cr	Ni	Al
6061-T6	0.93	0.25	0.15	0.62	0.7	0.1	0.25	−	Bal.
ER4047	0.04	0.11	0.09	12.15	0.38	0.07	−	−	Bal.

Table 2 Main deposition parameters

Sample No.	Arc current/A	Arc voltage/V	Wire feeding rate/(m·min^{-1})	Power composition/ wt.%	Powder feeding rate/ (g·min^{-1})
1#	125	18.2	6	100 Mg	0
2#	125	18.2	6	100 Mg	0.5
3#	125	18.2	6	100 Mg	1.7
4#	125	18.2	6	30Mg+70Ti	1.4

As shown in Fig. 1, the main experimental set-up includes a Fronius advanced welding power source, a VR 1550 CMT 4R/F++ wire feeder, a Fanuc M-710iC/50L 6-axis robot with a motion accuracy of ±0.07 mm, and a self-developed rotary double cylinder powder feeder. The powder feeding tube is a self-made copper tube with a diameter of 5 mm. During the WPAAM, the powder-leading was adopted as the deposition direction. To reduce the wire−powder feeding distance and improve the effective coupling of wire and powder, the sidewall of the protective sleeve of arc torch was ground, which decreased the wire−powder distance from 6 to 4 mm. According to the previous study [13], the fixed deposition parameters were optimized as follows: deposition speed of 10 mm/s, arc torch angle of 70°, powder feeding tube angle of 90°, wire-powder distance of 4 mm, and gas flow rate for powder feeding of 6 L/min. The main deposition parameters are listed in Table 2. The size of the deposited thin-wall was fixed as the length of 120 mm and the height of 30 mm. The width of deposited part varied with different deposition parameters. The multi-layer and single-pass deposition was accomplished by means of unidirectional repetition and layer-by-layer forming. To decrease the local heat accumulation on the forming quality of the deposited thin-wall, the next layer was fabricated after the temperature of previous deposited layer decreased to room temperature.

After the deposition, a digital camera was used to collect the macroscopic morphology of the deposited thin-wall, and the metallographic sample

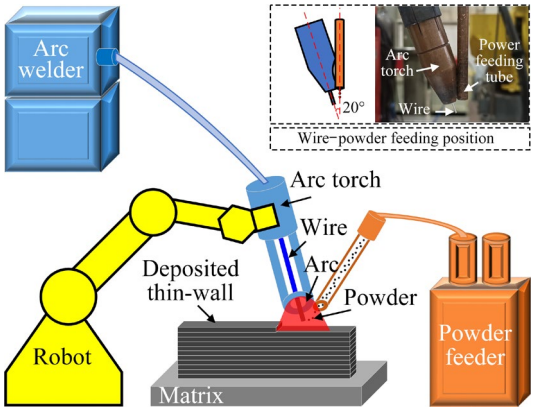

Fig. 1 Schematic diagram of experimental set-up

was prepared by a wire cut machine. The metallographic sample was then water-milled with 80#, 400#, 800#, 1000#, and 1200# sandpapers, and mechanically polished by diamond polishing pastes with particle sizes of W2.5 and W0.5, respectively. Before the microstructure observation, the metallographic samples were etched by Keller reagent containing 1 mL HF (40 wt.%), 1.5 mL HCl (37 wt.%), 2.5 mL HNO_3 (65 wt.%), and 95 mL H_2O. An Epson V39 scanner was used to collect the cross-sectional morphologies of the metallographic samples. An optical microscope (OM) and a scanning electron microscope (SEM) were employed to observe the microstructures. An X-ray diffraction (XRD) was used to analyze phase composition. The chemical composition of deposited parts was studied by an energy dispersive spectrometer (EDS) and an X-ray fluorescence spectrometer (XRF). Vickers microhardness of the deposited thin-wall was measured by a digitalized microhardness tester using a loading force of

1.96 N for 15 s. The tensile test samples were prepared by a wire cut machine with the dimensions shown in Fig. 2, and tested at room temperature. All the tensile test results were the average of at least three samples.

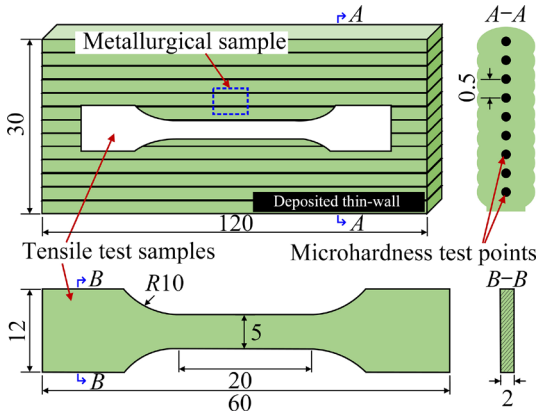

Fig. 2 Schematic drawing of tensile test samples and microhardness test points (unit: mm)

3 Results and discussion

3.1 Forming accuracy

As shown in Fig. 3(a), the deposited thin-wall (Sample 1#) obtained by the WAAM exhibits poor side flatness. Both the sags and bulges are found on the deposited surface. According to the cross-sectional morphology, the grooves between the deposited layers are quite deep, and there are some residual pores in the top area. As shown in Figs. 3(b) and (c), the surface forming accuracy of the thin-wall obtained based on the WPAAM is significantly improved. As the feeding rate of Mg powder (v_{Mg}) increases, the sidewall flatness becomes better, but some pores are still found inside the samples. To quantitatively describe the influence of added Mg powder on the forming accuracy of WAAMed thin-wall, this study defines the following parameters: Δh_1 and Δh_2 indicate re-melting depth, W_E and W_T are effective width and total width, respectively, η is effective width coefficient, and e is subsequent processing width. The calculations of η and e are based on Eqs. (1) and (2):

$$\eta=\frac{W_E}{W_T}\times 100\% \tag{1}$$

$$e=W_T-W_E \tag{2}$$

As shown in Fig. 3(d), the re-melting depth of WPAAM increases with increasing the v_{Mg}. When v_{Mg} is 0.5 g/min, the re-melting depth is increased by 43% compared with that of the WAAM without adding Mg powder. When v_{Mg} increases to 1.7 g/min, the re-melting depth can be increased by 95%, which indicates that the addition of Mg powder improves the concentration of arc combustion, thus increasing the penetration depth. As shown in Fig. 3(e), with increasing the addition of Mg powder, W_E increases, tends to be stable, and is improved by 38% relatively to the WAAM. Moreover, W_T gradually decreases. When v_{Mg} increases to 1.7 g/min, W_T is decreased by 16% relatively to the absence of Mg powder. To quantitatively describe the improvement of WAAM forming accuracy, η and e are calculated according to the Eqs. (1) and (2), respectively, as shown in Fig. 3(f). It can be found that increasing the addition of Mg powder causes the increase of η and the decrease of e, respectively. At the optimized v_{Mg} of 1.7 g/min, the effective deposition width of the WPAAM is increased by a maximum of 61% compared with that of the WAAM, and the machining allowance is reduced by a maximum of 81%. These quantitative results fully prove that the addition of Mg powder effectively improves the forming accuracy of WAAM.

3.2 Metallographic analysis results

The ER4047 aluminum alloy welding wire used in the deposition is a typical Al−Si casting aluminum alloy. Because the solubility of Si in Al is only 0.05% at room temperature, the eutectic Si precipitates during the cooling and solidification of Al−Si aluminum alloy. Therefore, as shown in Fig. 4(a), the basic constituent phases in the microstructure obtained by the WAAM include the α-Al matrix and Al−Si eutectic. After the repeated deposition of multi-layer and single-pass filling wire, the fusion line between the deposited layers of thin-wall is clearly visible. The typical structural characteristics include the remelted zone, heat-affected zone (HAZ), and arc fusion zone (hereinafter referred to as arc zone). The grains in the remelted zone are fine and the precipitated phase is small, while the eutectic Si in the HAZ is aggregated and grown up. As shown in Figs. 4(b) and (c), the microstructure of the thin-wall obtained by the WPAAM undergoes a series of changes relative to that by the WAAM. The number

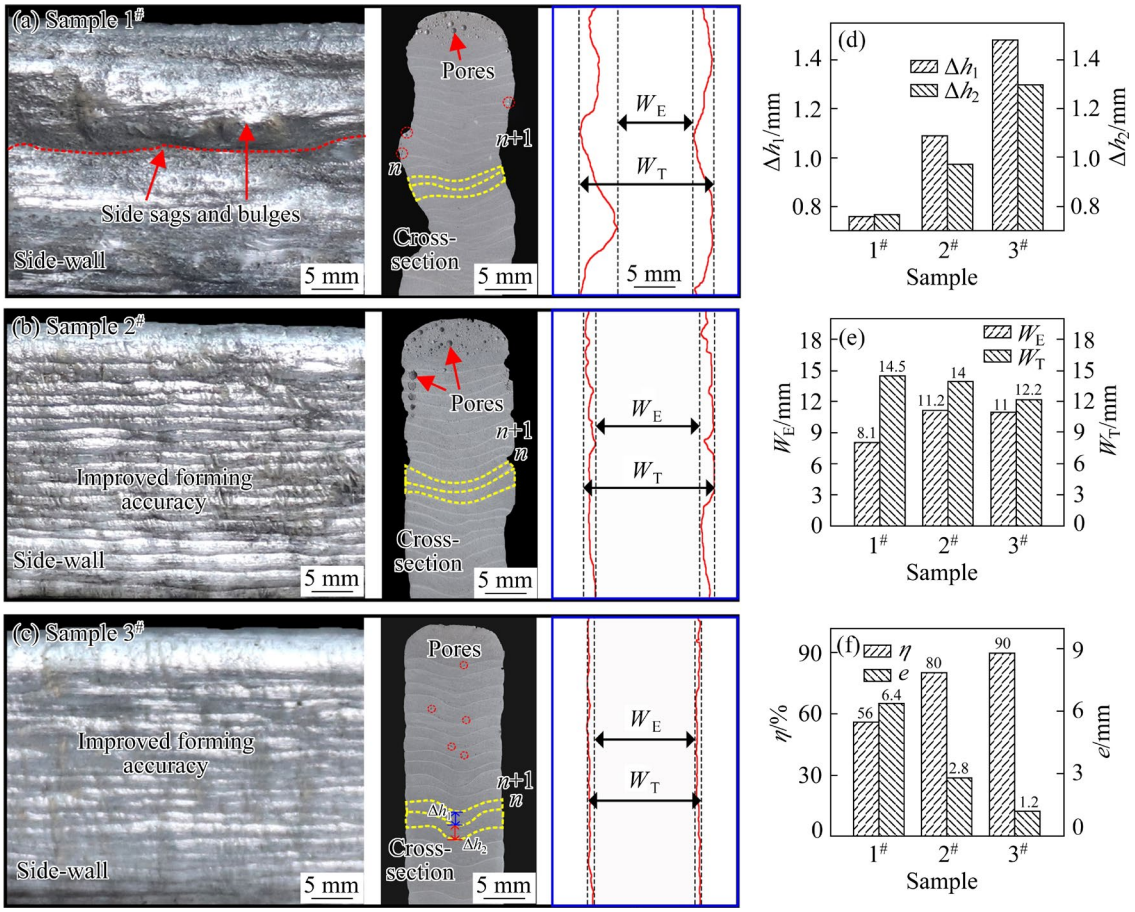

Fig. 3 Surface appearance and forming accuracy of deposited thin-wall: (a) Sample 1#; (b) Sample 2#; (c) Sample 3#; (d−f) Quantitative statistics of cross-sectional contours of different samples

of eutectic Si is significantly reduced, and more fine precipitates appear. When v_{Mg} increases from 0.5 to 1.7 g/min, the number of precipitates further increases.

To further identify the morphology and composition of the precipitated phase, the remelted zone was analyzed based on SEM, EDS and XRD tests shown in Figs. 5 and 6. The XRD results show that the Mg_2Si precipitated phase appears in the WPAAMed samples, which indicates that the filled Mg powder effectively enters the molten pool and metallurgically reacts with the Si element. As shown in Fig. 5(a), the eutectic Si in the WAAMed sample is mainly blocky distributed in the α-Al matrix, and obvious composition enrichment appears in some areas. The content of Si element is greatly increased compared with the original ER4047 aluminum alloy welding wire, which may be due to the repeated remelting of the wire. The redistribution and aggregation of Si element lead to the increase content in local areas. As shown in Figs. 5(b) and (c), when v_{Mg} is 0.5 g/min, in addition to eutectic Si, the new Mg_2Si precipitates are found in the deposited microstructures. When v_{Mg} increases to 1.7 g/min, the number of eutectic Si is further reduced, and the number of Mg_2Si is increased.

As shown in Fig. 7, the microstructure of WAAMed aluminum alloy is totally composed of the blocky columnar grains growing along the deposition direction, with an average grain size up to 61.83 μm. While many refined equiaxed grains appear in the WPAAMed aluminum alloy, and the average grain size is 47.1 μm, showing a decrease of 23.8% relatively to that of the WAAMed aluminum alloy. This indicates that the added Mg powder benefits to inhibit the growth of grains. According to the TEM analysis results of precipitates in the WPAAMed aluminum alloy, Mg element is detected in some precipitates and the area with Mg distribution also appears in the presence of Si, as shown in Fig. 8. The EDS and SAED further verify the existence of Mg_2Si new phase in the deposited microstructure.

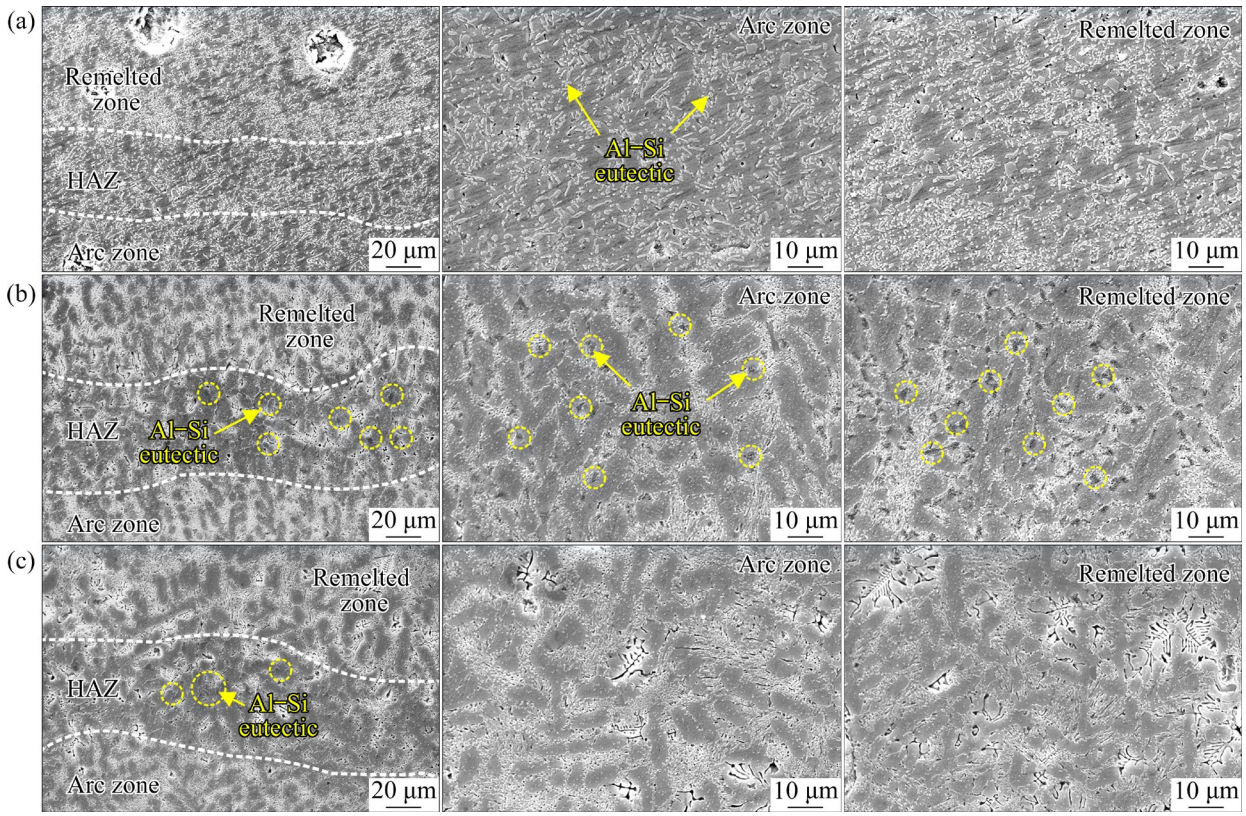

Fig. 4 Microstructure characteristics of deposited thin-wall: (a) Sample 1#; (b) Sample 2#; (c) Sample 3#

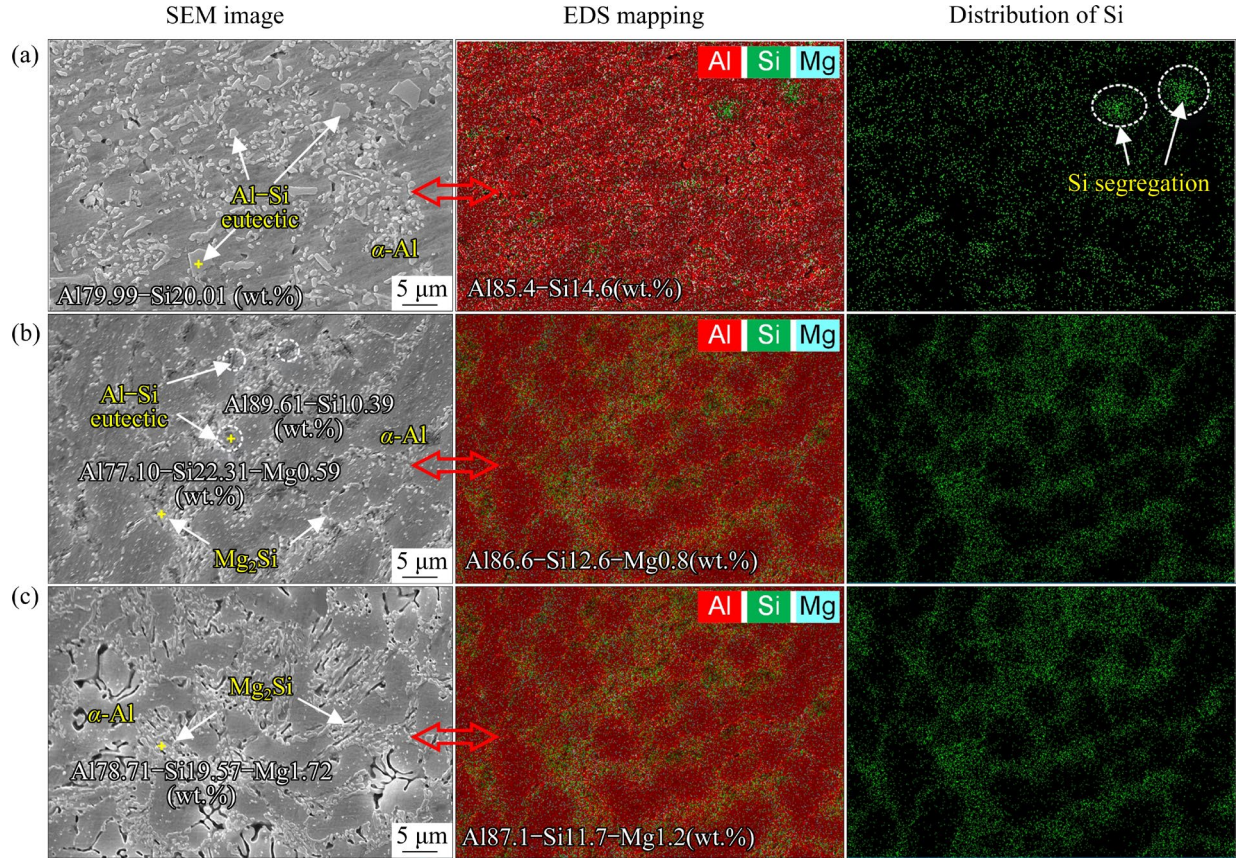

Fig. 5 EDS results in remelted zone of deposited thin-wall: (a) Sample 1#; (b) Sample 2#; (c) Sample 3#

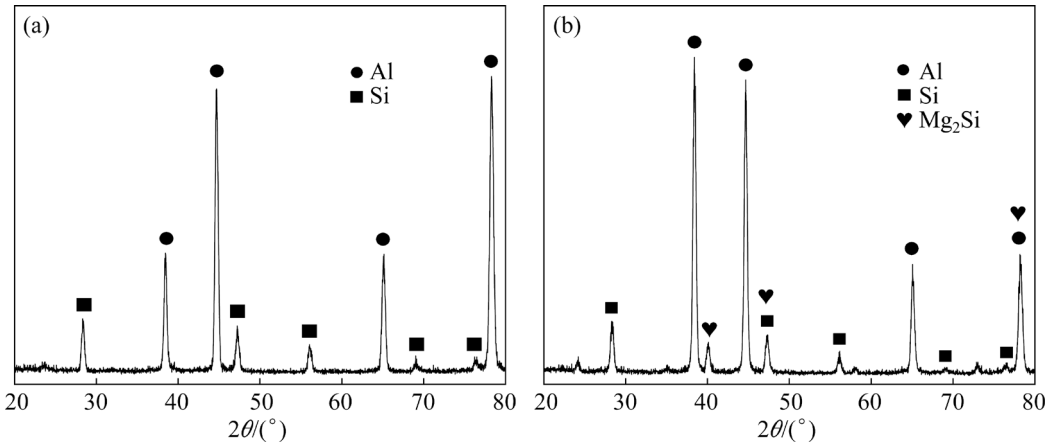

Fig. 6 XRD patterns of deposited thin-wall: (a) WAAM (Sample 1#); (b) WPAAM (Sample 3#)

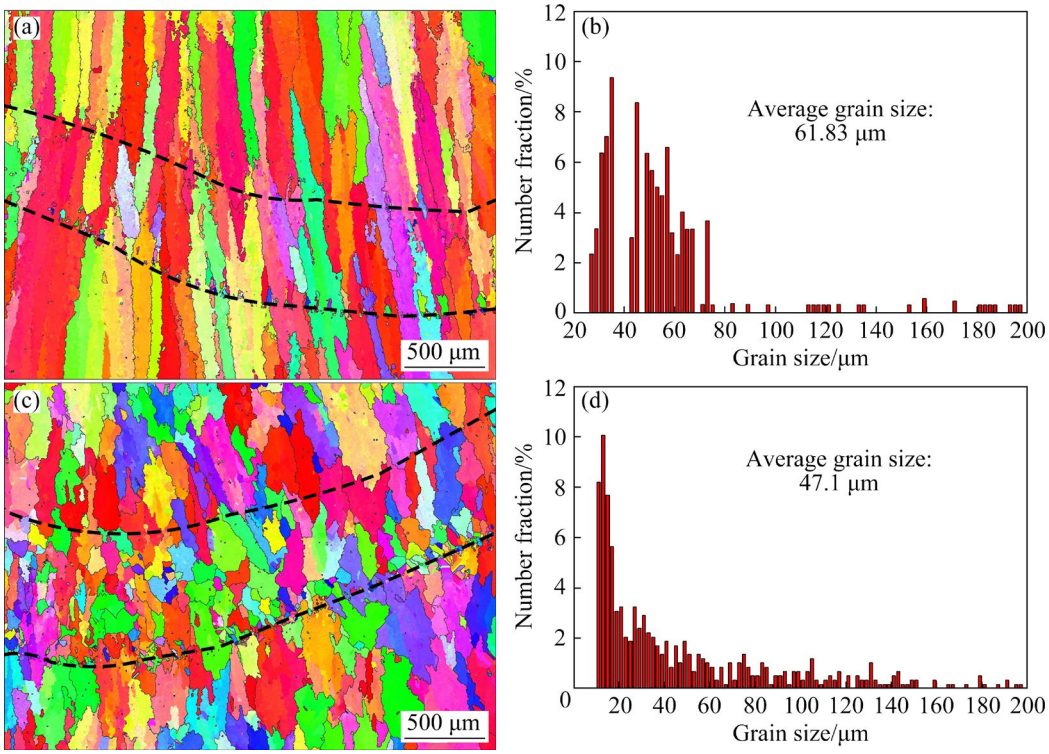

Fig. 7 EBSD results of deposited thin-wall: (a, b) WAAM (Sample 1#); (c, d) WPAAM (Sample 3#)

3.3 Mechanical properties

As shown in Fig. 9(a), the microhardness distribution of the WAAMed thin-wall is relatively low with an average value of HV 56.8, while the microhardness of the WPAAMed thin-wall is relatively high with an average value of HV 73.4, showing a 29% improvement. In addition, the maximum microhardness of the WPAAMed sample reaches up to HV 104.9, which is 50% higher than that of the WAAMed sample. Among them, the microhardness measurement value of some areas in the WPAAMed aluminum alloy is relatively low, which may be caused by the close measurement position to the pores existing in the deposited thin-wall. The reasons for the change of microhardness could be attributed to the following two points. On the one hand, the synchronous feeding of the wire and powder reduces the grain size of deposited microstructure. On the other hand, the added Mg powder reacts with eutectic Si to form a new Mg_2Si strengthening phases, which further improves the microhardness. Figure 9(b) shows the test results of tensile properties of deposited thin-walls. It can be seen that the tensile properties of the WAAMed thin-wall is higher than that of the WPAAMed, and the UTS and elongation

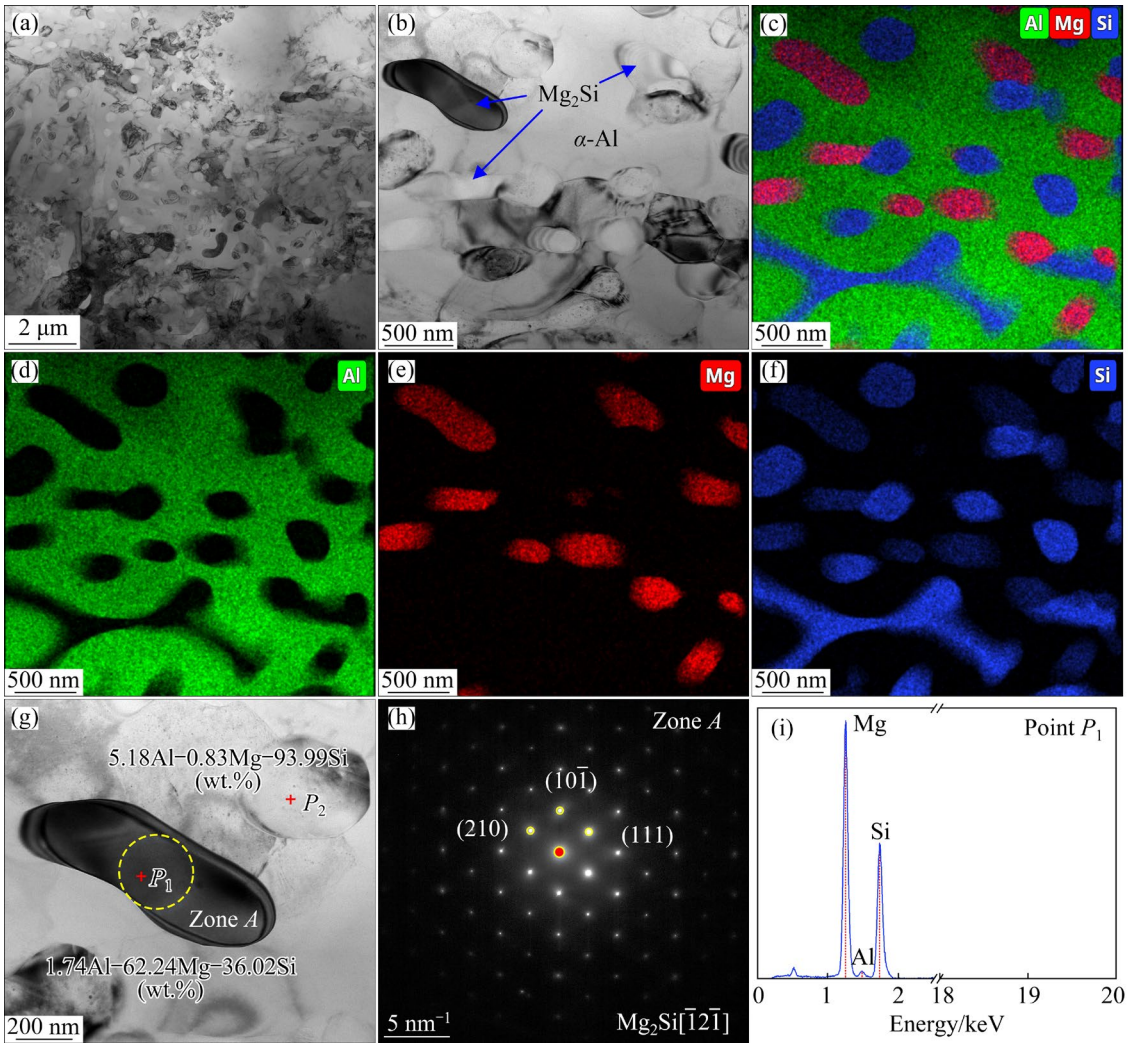

Fig. 8 TEM results of WPAAMed thin-wall (Sample 3#): (a, b) Morphologies of precipitates; (c–f) EDS mappings showing element distribution of Al, Mg and Si in (b); (g–i) Enlarged view and identification of Mg_2Si by SAED and EDS

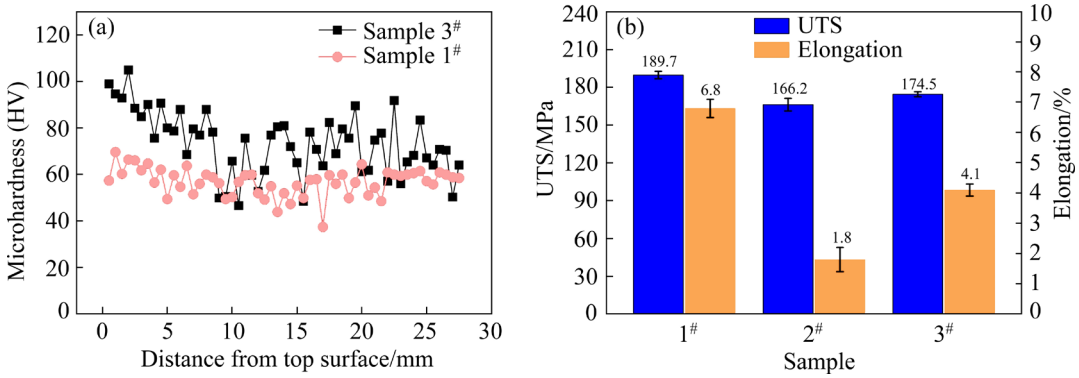

Fig. 9 Mechanical properties of deposited thin-wall: (a) Microhardness; (b) Tensile properties

are 189.7 MPa and 6.8% respectively. For the WPAAMed thin-wall, when v_{Mg} is 0.5 g/min, the UTS is 12% lower than that of WAAMed thin-wall, while the elongation is decreased by 74%. When v_{Mg} increases to 1.7 g/min, the UTS and elongation increase to 174.5 MPa and 4.1% respectively, reaching 92% and 60% those of the WAAMed deposited thin-wall, respectively.

Figure 10 shows macroscopic and microscopic morphologies of the tensile fracture of deposited

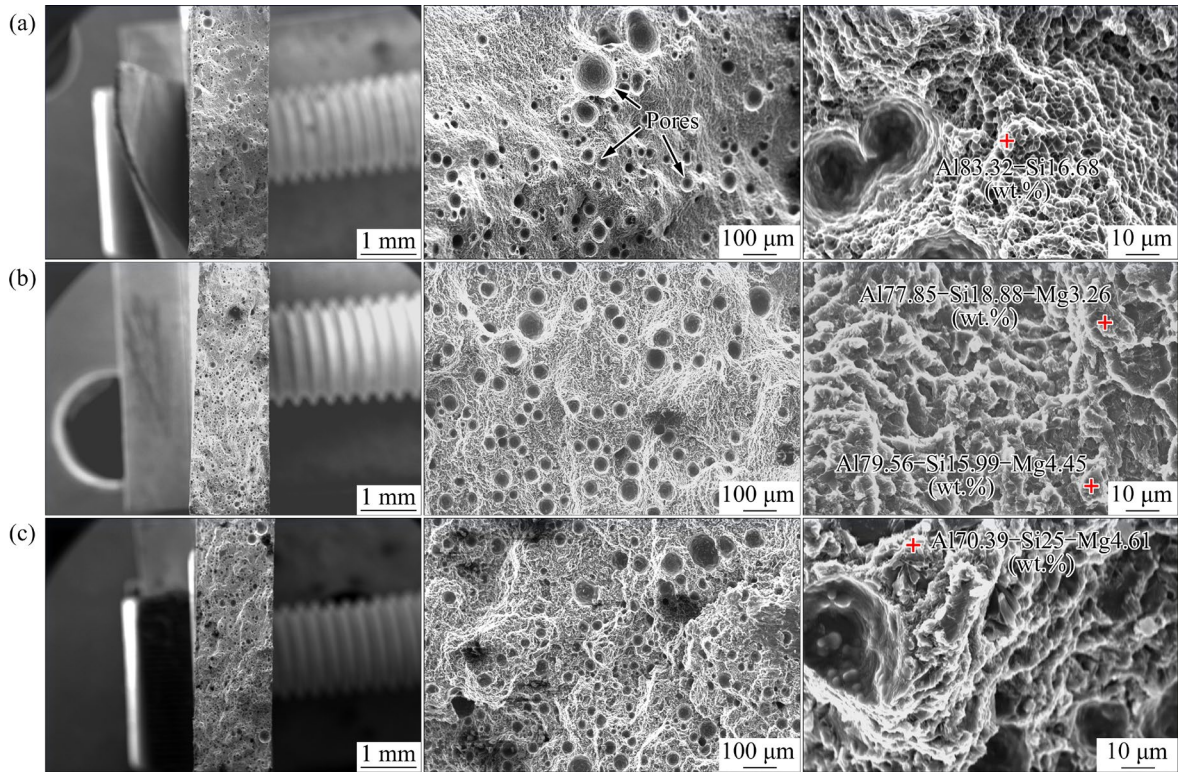

Fig. 10 Tensile fracture morphologies: (a) Sample 1#; (b) Sample 2#; (c) Sample 3#

thin-walls, as well as the corresponding EDS analysis results. The porosity on the fracture of the WAAM-deposited thin-wall is low and the size of pores is small. The tensile fracture mode conforms to the characteristics of ductile fracture, and typical dimples and tearing ridges appear on the fracture surface. The tensile cracks are mainly formed by the growth and aggregation of a large number of micropores in the microstructure under the action of tensile stress. The number of pores in the tensile fracture of WPAAM samples increases significantly. The inner wall of the pores mainly exhibits the spherical morphology with dendrites closely arranged, and the tensile fracture surface shows a mixed fracture mode of toughness and brittleness. This indicates that the high porosity induced by the addition of active Mg powder is the main reason for the decrease of the tensile properties of the WPAAMed thin-wall compared with the WAAMed thin-wall.

3.4 Influencing mechanism of Mg powder on WAAMed aluminum alloy

As shown in Fig. 11(a), the welding wire used in the deposition is a typical Al−Si aluminum alloy, which has the characteristics of low melting point and good fluidity. In addition, the Si content in the ER4047 aluminum alloy welding wire is relatively high (up to 12 wt.%), which further increases the fluidity of liquid metals. Moreover, the arc has the characteristics of low heat flux and large heating radius. The repeated movement of the arc heating during the additive manufacturing easily leads to the nonlinear time-varying characteristics of its thermal boundary conditions, uneven heat transfer, and arc root drift. Due to the high heat input, it is easy to cause the instability of molten pool, resulting in poor stability of the additive manufacturing and thus the poor forming accuracy of the deposited thin-wall. Previous studies [37,38] had shown that the driving force of molten pool affecting the WAAM mainly includes the following four types: electromagnetic force (E), Marangoni force (M), aerodynamic drag (A) and buoyancy (B). The behavior of molten pool is mainly affected by electromagnetic force and Marangoni force, while the influence of aerodynamic drag and buoyancy is very small and could be ignored. As shown in Fig. 11(b), when a sufficient amount of Mg powder is added during the WPAAM, the reason for the improved forming accuracy of WAAM can be attributed to the following aspects. First, under the

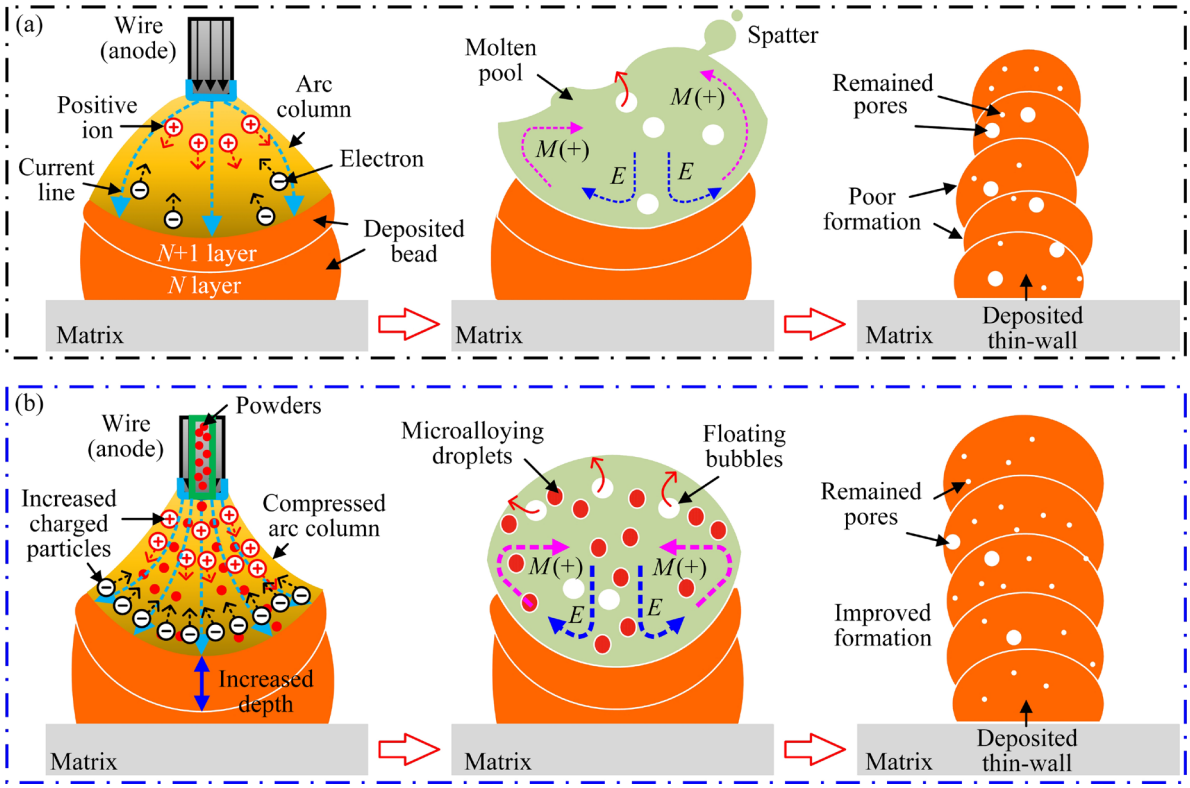

Fig. 11 Improvement mechanism of adding Mg powder on different WAAMed aluminum alloys: (a) WAAM; (b) WPAAM

action of high temperature of the arc, Mg is prone to ionization ($Mg=Mg^{2+}+2e$). As a result, the number of charged particles in the arc plasma increases and the arc column could be further compressed. Consequently, the arc itself is greatly concentrated and becomes more stable, which increases both the width and depth of the melted materials. Secondly, the added powder absorbs the heat and melts outside the arc, so the arc is further compressed and its energy is more concentrated. This improvement forms a great electromagnetic force on the molten pool, which enhances the fluidity of the liquid metals. Under the combined action of the above factors, the size of the molten pool formed by the WPAAM is larger than that of the WAAM, and the penetration depth of the deposited layer might be increased. Moreover, the enhanced melt flow promotes the molten metal to spread smoothly along the surface of the former deposited layer, and also promotes the escape of the formed bubbles and reduces the porosity after the solidification of molten pool. Furthermore, the added Mg powder easily vaporizes and forms metal vapor because of its low melting and boiling point, which also induces the formation of additional protection atmosphere around the arc. At the same time, the Mg element has a strong affinity for N and O elements, which reduces the adverse effect of external air intrusion on the molten pool. However, due to the addition of a large number of highly active Mg powders, a dense oxide film with strong water absorption still easily forms on the surface of the deposited layer. These impurities increase the hydrogen-containing impurities in the molten pool after the multiple re-melting of deposited metals, resulting in the formation of many hydrogen bubbles at the solid−liquid interface. It thus causes a significant increase in the porosity inside the deposited thin-wall. These residual pores seriously split the density between the grains of deposited microstructure and become an easy fracture area. This leads to the fact that the mechanical properties of the deposited thin-walls by the WPAAM are still not as good as those of the WAAMed thin-walls even if the new Mg_2Si strengthening phases are formed.

3.5 Reliability verification of large-sized deposition by WPAAM

To verify the feasibility and deposition stability of WPAAM for the fabrication of large-sized part, the deposition for a thin-wall with dimensions of

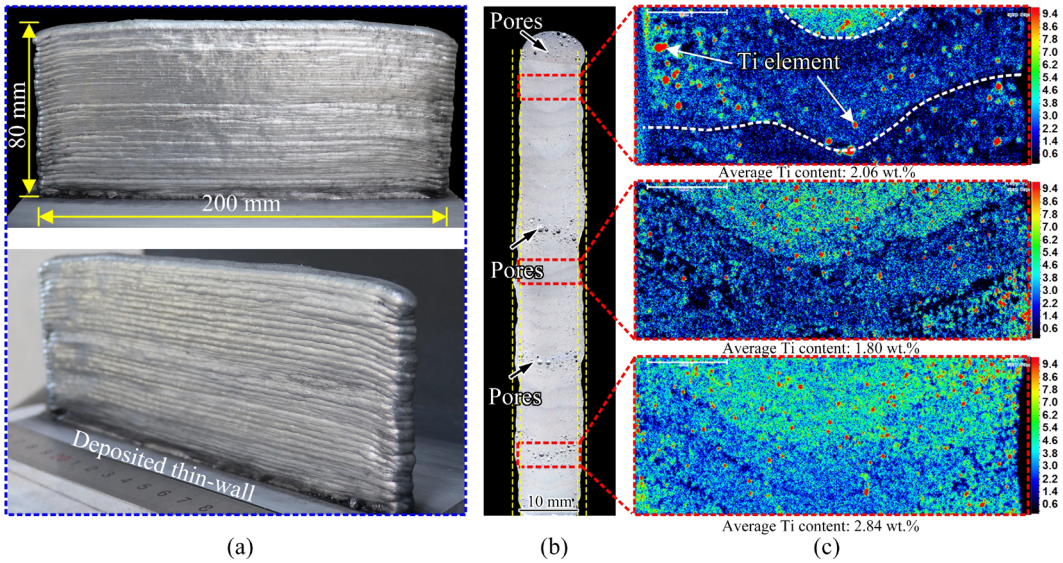

Fig. 12 Formation of deposited large-sized thin-wall by WPAAM, corresponding to Sample 4#: (a) Side-wall appearance; (b) Cross-section; (c) Distribution of Ti element

200 mm × 80 mm × 10 mm was carried out. In order to intuitively observe the distribution uniformity of powder composition in the deposited thin-wall, the pure Ti powders with higher melting point than that of Mg powders were used in the experiment. The large-sized thin-wall was formed using the mixed powders of 30Mg−70Ti (in wt.%). In addition, previous test results show that the inclined arc torch during the deposition easily causes the edge collapse of the deposited thin-wall. Therefore, the arc torch is turned to vertical and the powder feeding tube is inclined during the deposition. The other deposition parameters remain unchanged.

As shown in Fig. 12, the acceptable large-sized thin-wall is well formed, and its side surface is relatively flat. W_E and W_T are 8.8 and 11.4 mm, respectively. The calculated η and e are 77% and 2.6 mm, respectively. From the cross-sectional morphology of the thin-wall, there are still some residual pores in the sample, which are distributed in a chain shape. According to the XRF analysis results of the Ti element in the upper, middle and lower parts of the thin-wall, there is also a certain inhomogeneity in the distribution of element composition. The Ti content in the lower part of the sample is the highest, about 2.84 wt.%, and the distribution is the most uniform. While the Ti contents in the middle and upper parts of the sample are not much different, and are reduced nearly by 37%. The reason is that the cooling rate at the top of the deposited part is larger than that at the bottom, so the amount of powder effectively filled into the molten pool is reduced. This results in a decrease in the corresponding component content after the solidification of liquid metals. Furthermore, the distribution of Ti element in the upper part of the sample is obviously uneven compared with that in the lower part, and obvious Ti enrichment is found in the local area. The above results also show that the addition of powder has a significant effect on the forming accuracy of the WAAM, but it also brings both pore defects and uneven composition distribution. These problems are largely caused by the characteristics of the arc heat source and the material composition. It is still necessary to explore how to ensure the forming accuracy of the WPAMM and further improve the mechanical properties of the deposited thin-wall.

4 Conclusions

(1) Using the wire−powder arc additive manufacturing (WPAAM) based on the synchronous feeding of $AlSi_{12}$ wire and pure Mg powder, the high-efficiency and high-accuracy additive manufacturing of the target composition of Al−Si−Mg aluminum alloy was realized. At the optimized powder feeding rate of 1.7 g/min, the effective deposition width of the WPAAMed thin-wall was increased by 61% compared with that of the WAAMed thin-wall, and the machining

allowance was reduced by 81%.

(2) The adding of Mg powder at the optimized feeding rate benefited to inhibit the growth of columnar grains in the deposited microstructure, and form the refined equiaxed grains. The average grain size of thin-wall obtained by the WPAAM was 47.1 μm, showing a decrease of 23.8% relatively to that obtained by the WAAM. Moreover, the added Mg powders could react with the eutectic Si in the $AlSi_{12}$ wire to form a new Mg_2Si strengthening phase after the deposition.

(3) When the feeding rate of Mg powders increased from 0.5 to 1.7 g/min, the ultimate tensile strength and elongation of WPAAMed thin-wall increase to 174.5 MPa and 4.1%, respectively, reaching 92% and 60% those of the WAAMed thin-wall. However, the addition of highly active Mg powders also caused an increase of pores inside the deposited microstructure. These residual large pores seriously split the density between the grains and became the easiest area to fracture, which in turn decreased the mechanical properties of WPAAMed thin-wall.

CRediT authorship contribution statement

Yun-fei MENG: Conceptualization, Methodology, Formal analysis, Writing − Original draft; **Qian-xi YU:** Experimentation, Data Collection, Manuscript revision; **Xu WU:** Visualization, Resources, Supervision; **Ming GAO:** Validation, Funding acquisition; **Hui CHEN:** Project administration, Writing − Review & editing.

Declaration of competing interest

The authors declare that they have no known competing financial interests or personal relationships that could have appeared to influence the work reported in this paper.

Acknowledgments

The work was supported by the National Natural Science Foundation of China (No. 52205360)

References

[1] LIU Si-qi, WAN Di, PENG Ding, LU Xu, REN Xiao-bo, FU Yue-qun, WANG Feng, LI Yan-jun, ZHANG Zhi-ling, HE Jian-ying. Effect of heat input on nanomechanical properties of wire-arc additive manufactured Al 4047 alloys [J]. Materials Science and Engineering: A, 2022, 860: 144288.

[2] LUO Song, WEI Xiao-wei. A method for improving the mechanical properties of a hypereutectic Al−Si alloy by introducing the α-Al phase [J]. International Journal of Materials Research, 2016, 107(5): 422−428.

[3] DING Xue-ping, LI Dao-yuan, ZHANG Qi, MA Hong-lin, YANG Jie, FAN Shu-qian. Effect of ambient pressure on bead shape, microstructure and corrosion behavior of 4043 Al alloy fabricated by laser coaxial wire feeding additive manufacturing in vacuum environment [J]. Optics & Laser Technology, 2022, 153: 108242.

[4] WU J, WANG X Q, WANG W, ATTALLAH M M, LORETTO M H. Microstructure and strength of selectively laser melted AlSi10Mg [J]. Acta Materialia, 2016, 117: 311−320.

[5] LESPERANCE X, ILIE P, INCE A. Very high cycle fatigue characterization of additively manufactured AlSi10Mg and AlSi7Mg aluminium alloys based on ultrasonic fatigue testing [J]. Fatigue & Fracture of Engineering Materials & Structures, 2021, 44(3): 876−884.

[6] TANG Hua-ping, GAO Chao-feng, ZHANG Yong, ZHANG Nan-nan, LEI Chuan, BI Yun-jie, TANG Ping, RAO J H. Effects of direct aging treatment on microstructure, mechanical properties and residual stress of selective laser melted AlSi10Mg alloy [J]. Journal of Materials Science & Technology, 2023, 139: 198−209.

[7] LIU Tian-yu, MIN Xiao-hua, ZHANG Shuang, WANG Cun-shan, DONG Chuang. Microstructures and mechanical properties of Ti−Al−V−Nb alloys with cluster formula manufactured by laser additive manufacturing [J]. Transactions of Nonferrous Metals Society of China, 2021, 31: 3012−3023.

[8] LEE K H, YUN G J. A novel heat source model for analysis of melt pool evolution in selective laser melting process [J]. Additive Manufacturing, 2020, 36: 101497.

[9] DONG Ming-ye, ZHAO Yue, LI Quan, WANG Fu-de, WU Ai-ping. Effects of Cd addition in welding wires on microstructure and mechanical property of wire and arc additively manufactured Al−Cu alloy [J]. Transactions of Nonferrous Metals Society of China, 2022, 32: 750−764.

[10] MARTIN J, YAHATA B, HUNDLEY J, MAYER J, SCHAEDLER T, POLLOCK T. 3D printing of high-strength aluminium alloys [J]. Nature, 2017, 549: 365−369.

[11] ZHU Xing, ZHU Zhi-guang, LIU Ting-ting, LIAO We-he, DU Yu-lei, WEI Hui-liang. Crack-free and high-strength AA2024 alloy obtained by additive manufacturing with controlled columnar-equiaxed-transition [J]. Journal of Materials Science & Technology, 2023, 156: 183−196.

[12] MENG Yun-fei, LI Jian, ZHANG Shuai, GAO Ming, GONG Meng-cheng, CHEN Hui. Wire arc additive manufacturing of Ni−Al intermetallic compounds through synchronous wire-powder feeding [J]. Journal of Alloys and Compounds, 2023, 943: 169152.

[13] MENG Yun-fei, LI Ze-yu, GAO Ming, CHEN Hui, ZHANG Chen. Parameter optimization and mechanism of synchronous wire-powder arc melting deposition of aluminum alloy [J]. Journal of Materials Engineering and Performance, 2024, 33(5): 2488−2501.

[14] KEMPEN K, THIJS L, HUMBEECK J, KRUTH J. Mechanical properties of AlSi10Mg produced by selective

laser melting [J]. Physics Procedia, 2012, 39: 439−446.

[15] READ N, WANG W, ESSA K, ATTALLAH M M. Selective laser melting of AlSi10Mg alloy: Process optimization and mechanical properties development [J]. Materials & Design, 2015, 65: 417−424.

[16] YAN Qian, SONG Bo, SHI Yu-sheng. Comparative study of performance comparison of AlSi10Mg alloy prepared by selective laser melting and casting [J]. Journal of Materials Science & Technology, 2020, 41: 199−208.

[17] LIU Yang, LIU Chao, LIU Wen-sheng, MA Yun-zhu, TANG Si-wei, LIANG Chao-ping, CAI Qing-shan, ZHANG Cheng. Optimization of parameters in laser powder deposition AlSi10Mg alloy using Taguchi method [J]. Optics & Laser Technology, 2019, 111: 470−480.

[18] FRAZIER W E. Metal additive manufacturing: A review [J]. Journal of Materials Engineering and Performance, 2014, 23: 1917−1928.

[19] KOTADIA H, GIBBONS G, DAS A, HOWES P D. A review of laser powder bed fusion additive manufacturing of aluminium alloys: Microstructure and properties [J]. Additive Manufacturing, 2021, 46: 102155.

[20] XIONG Yi-bo, WEN Dong-xu, ZHENG Zhi-zhen, LI Jian-jun. Effect of interlayer temperature on microstructure evolution and mechanical performance of wire arc additive manufactured 300M steel [J]. Materials Science and Engineering: A, 2022, 831: 142351.

[21] LI Yan-peng, WANG Chang-rui, DU Xiao-dong, TIAN Wei, ZHANG Tao, HU Jun-shan, LI Bo, LI Peng-cheng, LIAO Wen-he. Research status and quality improvement of wire arc additive manufacturing of metals [J]. Transactions of Nonferrous Metals Society of China, 2023, 33: 969−996.

[22] HEJRIPOUR F, VALENTINE D T, AIDUN D K. Study of mass transport in cold wire deposition for wire arc additive manufacturing [J]. International Journal of Heat and Mass Transfer, 2018, 125: 471−484.

[23] HAN Qing-lin, GAO Jia, HAN Chang-le, ZHANG Guang-jun, LI Yong-zhe. Experimental investigation on improving the deposition rate of gas metal arc-based additive manufacturing by auxiliary wire feeding method [J]. Welding in the World, 2021, 65(1): 35−45.

[24] WANG He, MA Shu-yuan, WANG Jia-chen, LU Tao, LIU Chang-meng. Microstructure and mechanical properties of TA15/TC11 graded structural material by wire arc additive manufacturing process [J]. Transactions of Nonferrous Metals Society of China, 2021, 31: 2323−2335.

[25] WEN Dong-xu, LONG Ping, LI Jian-jun, HUANG Liang, ZHENG Zhi-zhen. Effects of linear heat input on microstructure and corrosion behavior of an austenitic stainless steel processed by wire arc additive manufacturing [J]. Vacuum, 2020, 173: 109131.

[26] JAFARI D, VANEKER T, GIBSON I. Wire and arc additive manufacturing: Opportunities and challenges to control the quality and accuracy of manufactured parts [J]. Materials & Design, 2021, 202: 109471.

[27] CUNNINGHAM C R, FLYNN J M, SHOKRANI A, DHOKIA V, NEWMAN S T. Invited review article: Strategies and processes for high quality wire arc additive manufacturing [J]. Additive Manufacturing, 2018, 22: 672−686.

[28] SUN Guo-qin, ZHU Dong-yue, CHEN Shu-jun, DENG Zhan-feng, KANG Wei, SHANG De-guang. Fatigue crack initiation and propagation of wire arc additive manufactured Al−Mg alloy [J]. Engineering Failure Analysis, 2023, 148: 107164.

[29] SURYAKUMAR S, KARUNAKARAN K P, BERNARD A, CHANDRASEKHAR U, RAGHAVENDER N, SHARMA D. Weld bead modeling and process optimization in hybrid layered manufacturing [J]. Computer-Aided Design, 2011, 43(4): 331−344.

[30] QI Ze-wu, QI Bo-jin, CONG Bao-qiang, ZHANG Rui-ze. Microstructure and mechanical properties of wire + arc additively manufactured Al−Mg−Si aluminum alloy [J]. Materials Letters, 2018, 233: 348−350.

[31] YU Zhan-liang, YUAN Tao, XU Min, CHEN Shu-jun. Microstructure and mechanical properties of Al−Zn−Mg−Cu alloy fabricated by wire + arc additive manufacturing [J]. Journal of Manufacturing Processes, 2021, 62: 430−439.

[32] MENG Yun-fei, GAO Ming, ZENG Xiao-yan. Effects of arc types on the laser-arc synergic effects of hybrid welding [J]. Optics Express, 2018, 26(11): 14775−14785.

[33] XIA Chun-yang, PAN Zeng-xi, POLDEN J, LI Hui-jun, XU Yang-ling, CHEN Shan-ben, ZHANG Yu-ming. A review on wire arc additive manufacturing: Monitoring, control and a framework of automated system [J]. Journal of Manufacturing Systems, 2020, 57: 31−45.

[34] MENG Yun-fei, GAO Ming, ZENG Xiao-yan. Quantitative analysis of synergic effects during laser-arc hybrid welding of AZ31 magnesium alloy [J]. Optics and Lasers in Engineering, 2018, 111: 183−192.

[35] MENG Yun-fei, GONG Meng-cheng, ZHANG Shuai, ZHANG Ya-zhou, GAO Ming. Effects of oscillating laser offset on microstructure and properties of dissimilar Al/steel butt-joint [J]. Optics and Lasers in Engineering, 2020, 128, 106037.

[36] WU De-fan, CUI Li, WU Xu, GUO Xing-ye, SHAO Wei, TAN Zhen, HE Ding-yong. Cold metal transfer welding of AlSi7Mg alloy sheets prepared by selective laser melting [J]. Journal of Manufacturing Processes, 2022, 84: 282−297.

[37] LI Geng, ZHANG Chen, GAO Ming, ZENG Xiao-xia. Role of arc mode in laser-metal active gas arc hybrid welding of mild steel [J]. Materials & Design, 2014, 61: 239−250.

[38] MENG Yun-fei, LI Geng, GAO Ming, ZHANG Chen, ZENG Xiao-yan. Formation and suppression mechanism of lack of fusion in narrow gap laser-arc hybrid welding [J]. The International Journal of Advanced Manufacturing Technology, 2019, 100: 2299−2309.

基于丝粉同步沉积的 Al−Si−Mg 铝合金电弧增材制造工艺

孟云飞[1,2]，余千禧[1,2]，伍 旭[1,2]，高 明[3]，陈 辉[1,2]

1. 西南交通大学 材料科学与工程学院，成都 610031；
2. 西南交通大学 材料先进技术教育部重点实验室，成都 610031；
3. 华中科技大学 武汉光电国家研究中心，武汉 430074

摘 要：因为缺乏匹配的商用化焊丝，多数铝合金的电弧熔丝增材制造(WAAM)发展受阻。本文作者采用丝粉同步电弧增材制造技术(WPAAM)制备 Al−Si−Mg 铝合金。基于 $AlSi_{12}$ 焊丝和纯 Mg 粉的同步沉积，采用 WPAAM 工艺得到薄壁墙的有效宽度相比基于 $AlSi_{12}$ 焊丝沉积的 WAAM 提高了 61%，而且其加工余量减少了 81%。Mg 粉的添加有利于沉积组织中形成细化的等轴晶，使得 WPAAM 薄壁墙的平均晶粒尺寸减小至 47.1 μm，相对于 WAAM 的减小了 23.8%。此外，Mg 还能与 Si 元素反应生成新的 Mg_2Si 强化相。力学性能测试结果表明，WPAAM 沉积薄壁墙的抗拉强度和伸长率为 174.5 MPa 和 4.1%，分别达到 WAAM 的 92%和 60%。

关键词：电弧增材制造；丝粉同步沉积；Al−Si−Mg 铝合金；成形精度；力学性能

(Edited by Wei-ping CHEN)